Available online at www.sciencedirect.com
ScienceDirect
Energy Reports 8 (2022) 650–657
www.elsevier.com/locate/egyr

2022 The 5th International Conference on Renewable Energy and Environment Engineering (REEE 2022), 24–26 August, 2022, Brest, France

Sensorless control of IPMSM using a discrete-time super twisting observer by high-frequency current injection in low speed region

Z. Xu[a,*], Chris Gerada[b]

[a] University of Nottingham, Ningbo 315105, China
[b] University of Nottingham, Nottingham NG72RD, UK

Received 6 October 2022; accepted 8 October 2022
Available online 25 October 2022

Abstract

Control of interior permanent magnet synchronous motors (IPMSMs) has been extensively attempted without any position sensor. At extremely low speeds, sensorless operation would not rely on the fundamental model-based sensorless methods since the situation becomes more sophisticated. The existing high-frequency (HF) injection techniques predominantly concentrate on current or voltage excitations. Whereas, compromises are made between the signal strength and inevitably generated current fluctuations and torque ripples. Noise and disturbances could also deteriorate the performance. To accomplish the low speed sensorless operation successfully, this paper presents a position error observer and a current injection scheme for the extremely low speed sensorless operation. A discrete-time super twisting extended-state observer (STESO) extracts the estimated position and speed considering the disturbances. The design of the HF observer is carried out. The lowest speed is extended down to 2% rated value in the experimental tests.

Peer-review under responsibility of the scientific committee of the 5th International Conference on Renewable Energy and Environment Engineering, REEE, 2022.

Keywords: IPMSM; Sensorless control; High-frequency current injection

1. Introduction

IPMSM is more applicable for traction applications with electric drive systems, which require flux-weakening operation and high torque density. Various studies and mature commercialization on the IPMSMs have been performed, due to their advantages on high power density and efficiency, low torque ripple, high dynamic performance and minimal maintenance requirements.

Research studies focusing on sensorless control (SC) methods are gaining appealing due to the concerns. Such techniques are also referred to as self-sensing or encoderless, which only utilizes the electrical measurements to estimate the rotor position and rotor speed without using any position sensor. In the sensorless operation, the SC without the position sensor plays a vital role in the condition that the position sensor gets faulty or fails, to ensure

* Corresponding author.
E-mail address: zhuang.xu@nottingham.edu.cn (Z. Xu).

https://doi.org/10.1016/j.egyr.2022.10.166

Peer-review under responsibility of the scientific committee of the 5th International Conference on Renewable Energy and Environment Engineering, REEE, 2022.

the safety and high performance operation of the motor. At present, the effect of electromagnetic saturation and the slot harmonic components due to the rotor position increase the position estimation error, leading to mechanical vibration, even with no load. Those bring great challenges to SC. Generally, SC techniques are categorized into two major divisions [1–9]: (1). Rotor saliency based methods using high-frequency signal injection [1–3,5]. (2). Fundamental excitation techniques [4,6,7,9].

If the operating speed is extremely low, the SC operation cannot rely on the model-based estimation methods alone. Since the EMF is very small at low rotor speed and the ratio of the signal to noise is low, the model-based methods will lose performance. For the previously proposed sensorless control method associated with STESO, the minimum reachable speed was 89 rpm without compensation or signal injection. Hence, in this paper, the low speed operation will be dealt with specifically.

As mentioned previously, the HF injection methods feature with specialty at low speed, which can be adopted to complete the low speed range operation. In conventional HF model, the voltage drops on stator resistance and the speed related terms are usually neglected when the injection frequency is high enough. However, such model may not be precise and higher injection frequency will result in higher motor loss. In the conventional methods [3], the HF sinusoidal voltage with a constant amplitude is usually directly injected to the reference voltage which may degrade the performance under various operating conditions or interfere with the existing control loop, when the injection frequency is limited and gets closer to the fundamental frequency. Besides, the extraction of the rotor position is calculated based on the negative-sequence current components which may be sensitive and vulnerable to disturbance.

In this paper, a high-frequency extended EMF model without neglecting the resistance and speed terms is adopted. A superimposition of a HF rotating current with a moderate frequency is injected in the IPMSM to generate and retrieve the rotor position information with saliency. The amplitude of the HF current is controlled to a small constant by a HF current controller to ensure the stability of the existing IPMSM drive system. The solution of separating the two current control systems prevents the superimposed HF components interfering from the existing current control loop. Adopting the HF model, a HF adaptive observer is proposed to estimate the excited extended EMF. The HF observer can be conveniently converted and redesigned from the fundamental frequency front end observer because it provides satisfactory estimation performance. Since the estimated EMF contains the combination of HF switching and fundamental components, the fundamental components need to be extracted by the heterodyne method and fed to the back-end observer. Hence, by using the unified sensorless structure with the proposed STESO, the extremely low speed operation can be achieved.

2. Modeling of IPMSM in the estimated rotating frame

In the sensorless operations, the actual rotor angle θ_{re} is not directly measured by any position sensor. The orientation of the synchronous d–q coordinate is unknown. Instead, the flux and torque components of the controlled current vector are decoupled in the γ–δ axis estimated by sensorless schemes.

In the d–q rotating frame, the voltage equation of IPMSMs is governed by

$$\boldsymbol{v_{dq}} = \boldsymbol{Z i_{dq}} + \boldsymbol{e} \tag{1}$$

where $\boldsymbol{v_{dq}} = \begin{bmatrix} v_d & v_q \end{bmatrix}^T$ is the d–q axis stator voltage vector. $\boldsymbol{i_{dq}} = \begin{bmatrix} i_d & i_q \end{bmatrix}^T$ is the d–q stator current vector. $\boldsymbol{e} = \begin{bmatrix} 0 & K_E \omega_r \end{bmatrix}^T$. K_E is back EMF constant. The impedance $\boldsymbol{Z}$ is

$$\boldsymbol{Z} = \begin{bmatrix} R + pL_d & -\omega_r L_q \\ \omega_r L_d & R + pL_q \end{bmatrix} \tag{2}$$

where R stands for the stator resistance, L_d and L_q are the inductances. p is the differential operator d/dt.

The estimation error $\tilde{\theta}$ of the rotor position is the shift between the γ–δ coordinate and the d–q reference frame. $\tilde{\theta} = \theta_{re} - \hat{\theta}_{re}$ where $\hat{\theta}_{re}$ is the estimated rotor position. Multiplying the rotation matrix $e^{J\tilde{\theta}}$ enables Eq. (1) to go from d–q axis into the γ–δ reference frame.

$$\boldsymbol{v_{\gamma\delta}} = \boldsymbol{Z_{\gamma\delta} i_{\gamma\delta}} + \boldsymbol{e_{\gamma\delta}} \tag{3}$$

where the γ–δ axis vectors $\boldsymbol{v}_{\gamma\delta}$, $\boldsymbol{i}_{\gamma\delta}$, $\boldsymbol{e}_{\gamma\delta}$ and $\boldsymbol{Z}_{\gamma\delta}$ are defined as follows. $\boldsymbol{v}_{\gamma\delta} = \begin{bmatrix} v_\gamma & v_\delta \end{bmatrix}^T$; $\boldsymbol{i}_{\gamma\delta} = \begin{bmatrix} i_\gamma & i_\delta \end{bmatrix}^T$; $\boldsymbol{e}_{\gamma\delta} = \begin{bmatrix} -K_E\omega_r sin(\tilde{\theta}) & K_E\omega_r cos(\tilde{\theta}) \end{bmatrix}^T$ and

$$\boldsymbol{Z}_{\gamma\delta} = \begin{bmatrix} R + \hat{\omega}_r L_{\gamma\delta} + pL_\gamma & -\hat{\omega}_r L_\delta - pL_{\gamma\delta} \\ \hat{\omega}_r L_\gamma - pL_{\gamma\delta} & R - \hat{\omega}_r L_{\gamma\delta} + pL_\delta \end{bmatrix} \tag{4}$$

where $L_\gamma = 1/2[\left(L_d + L_q\right) - \left(L_q - L_d\right) cos\left(2\tilde{\theta}\right)]$; $L_\delta = 1/2[\left(L_d + L_q\right) + \left(L_q - L_d\right) cos\left(2\tilde{\theta}\right)]$; $L_{\gamma\delta} = 1/2\left(L_q - L_d\right) sin(2\tilde{\theta})$.

3. Estimation error of the rotor position

In this Section, the position estimation error $\tilde{\theta}$ is observed by an extended *Luenberger* observer (ELO). The observer takes on the role of detecting the phase angle of the rotor position by forming an error correction term. If $\tilde{\theta}$ is sufficiently small, in (3), $L_\gamma \cong L_d$, $L_\delta \cong L_q$ and $L_{\gamma\delta} \cong 0$. $\boldsymbol{Z}_{\gamma\delta}$ becomes

$$\boldsymbol{Z}_{\gamma\delta 0} = \begin{bmatrix} R + pL_d & -\hat{\omega}_r L_q \\ \hat{\omega}_r L_d & R + pL_q \end{bmatrix} \tag{5}$$

A current model of IPMSMs is established by re-writing (3) as

$$d\boldsymbol{i}_{\gamma\delta}/dt = \boldsymbol{Z}_0\boldsymbol{i}_{\gamma\delta} + \boldsymbol{L}_0\boldsymbol{e}_{\gamma\delta} + \boldsymbol{v}_0 \tag{6}$$

where $\boldsymbol{Z}_0 = \begin{bmatrix} -R/L_d & \hat{\omega}_r L_q/L_d \\ -R/L_q & -\hat{\omega}_r L_d/L_q \end{bmatrix}$, $\boldsymbol{L}_0 = \begin{bmatrix} -1/L_d & 0 \\ 0 & -1/L_q \end{bmatrix}$ and $\boldsymbol{v}_0 = \begin{bmatrix} v_\gamma/L_d & v_\delta/L_q \end{bmatrix}^T$. An extended state is defined to treat the derivative of $\boldsymbol{e}_{\gamma\delta}$ as disturbance. $\dot{\boldsymbol{e}}_{\gamma\delta} = w(t)$. Assuming that $w(t)$ is bounded, The current model (6) is re-arranged as:

$$\begin{cases} d\boldsymbol{i}_{\gamma\delta}/dt = \boldsymbol{Z}_0\boldsymbol{i}_{\gamma\delta} + \boldsymbol{L}_0\boldsymbol{e}_{\gamma\delta} + \boldsymbol{v}_0 \\ d\boldsymbol{e}_{\gamma\delta}/dt = w(t) \end{cases} \tag{7}$$

An ELO is constructed based on (7) to track $\tilde{\theta}$ that is hidden in $\boldsymbol{e}_{\gamma\delta}$ term.

$$\begin{cases} d\hat{\boldsymbol{i}}_{\gamma\delta}/dt = \boldsymbol{Z}_0\boldsymbol{i}_{\gamma\delta} + \boldsymbol{L}_0\hat{\boldsymbol{e}}_{\gamma\delta} + \boldsymbol{v}_0 - \boldsymbol{L}_{o1}(\hat{\boldsymbol{i}}_{\gamma\delta} - \boldsymbol{i}_{\gamma\delta}) \\ d\hat{\boldsymbol{e}}_{\gamma\delta}/dt = -\boldsymbol{L}_{o2}(\hat{\boldsymbol{i}}_{\gamma\delta} - \boldsymbol{i}_{\gamma\delta}) \end{cases} \tag{8}$$

where $\hat{\boldsymbol{i}}_{\gamma\delta} = \begin{bmatrix} \hat{i}_\gamma & \hat{i}_\delta \end{bmatrix}^T$. The quantities with the hat on top indicate the current estimates. $\hat{\boldsymbol{e}}_{\gamma\delta} = \begin{bmatrix} -\hat{g}_1 & \hat{g}_2 \end{bmatrix}^T$. $\hat{g}_1$ tracks $K_E\omega_r sin\left(\tilde{\theta}\right)$ and $\hat{g}_2$ is the estimate of $K_E\omega_r cos(\tilde{\theta})$. After the observer gains $\boldsymbol{L}_{o1}$ and $\boldsymbol{L}_{o2}$ are configured properly, $\hat{g}_1$ and $\hat{g}_2$ will converge to their actual values. As soon as $\hat{\boldsymbol{e}}_{\gamma\delta}$ gets closer to $\boldsymbol{e}_{\gamma\delta}$, $\tilde{\theta}$ is obtained by calculating (9)

$$sin\left(\tilde{\theta}\right) = \hat{g}_1/\sqrt{\hat{g}_1^2 + \hat{g}_2^2} \tag{9}$$

The convergence of (8) is guaranteed by verifying the error dynamics and proving the stability [9]. Fig. 1 shows the overview of ELO's structure.

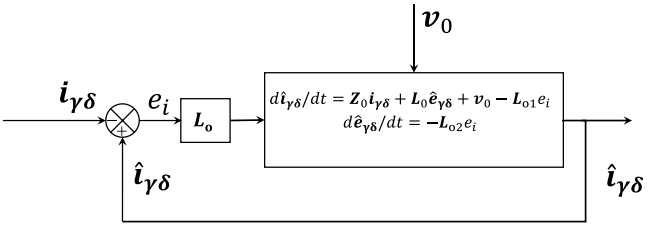

Fig. 1. Construction of ELO for position error estimation.

4. High-frequency current injection and estimation of extended EMF, rotor position and speed

4.1. High-frequency current injection

At extremely low speeds, the HF current components are superimposed in the rotating frame or stationary frame.

$$i_h = \begin{bmatrix} i_{h\gamma} \\ i_{h\delta} \end{bmatrix} = \begin{bmatrix} i_{h\alpha} \\ i_{h\beta} \end{bmatrix} \tag{10}$$

A HF current controller needs to be adopted to maintain the super-imposed HF current components at an appropriate level in the system. The diagram of the sensorless control system with HF injection in shown in Fig. 3. The control reference value of the rotating injection current is annotated as $i^*_{h\gamma}$ and $i^*_{h\delta}$, which is defined as

$$\begin{bmatrix} i^*_{h\gamma} \\ i^*_{h\delta} \end{bmatrix} = \left|i^*_h\right| \begin{bmatrix} \cos \omega_h t \\ \sin \omega_h t \end{bmatrix} \tag{11}$$

where ω_h is the rotating speed of the HF injection current and $\left|i^*_h\right|$ is the amplitude of the injection current. The HF excited extended EMFs expressed in (12) are estimated by using a sliding adaptive observer [8] incorporating HF components.

$$\hat{e}_h = \begin{bmatrix} \hat{e}_{h\alpha} \\ \hat{e}_{h\beta} \end{bmatrix} \tag{12}$$

Substituting (10) into the definition of the extended EMF [8], the estimated HF extended EMF can be written as

$$\begin{bmatrix} \hat{e}_{h\alpha} \\ \hat{e}_{h\beta} \end{bmatrix} = \left\{ \left(L_d - L_q\right) \left[\left(\omega_{re} - \omega_h\right) |i_h| \cos \omega_h t \right] + \omega_{re} K_E \right\} \begin{bmatrix} -\sin \theta_{re} \\ \cos \theta_{re} \end{bmatrix} \tag{13}$$

Since (13) contains the multiplication of HF components and fundamental components, heterodyne method is needed to extract the fundamental signals. By multiplying the HF component $\cos \omega_h t$, Eq. (13) can be converted into the following expression.

$$\begin{bmatrix} \hat{e}_{h\alpha} \\ \hat{e}_{h\beta} \end{bmatrix} \cos \omega_h t = \left\{ \left(L_d - L_q\right) \left[\left(\omega_{re} - \omega_h\right) |i_h| \frac{\left(\cos 2\omega_h t + 1\right)}{2} \right] + \omega_{re} K_E \cos \omega_h t \right\} \begin{bmatrix} -\sin \theta_{re} \\ \cos \theta_{re} \end{bmatrix} \tag{14}$$

Since the frequency of HF injection components is much higher than the fundamental one at low speed, a bandpass filter can be used to extract the fundamental extended EMF. The extracted extended EMF at the front-end is represented as

$$\begin{bmatrix} \hat{e}_{\alpha} \\ \hat{e}_{\beta} \end{bmatrix} = \left\{ \left(L_d - L_q\right) \left[\frac{\left(\omega_{re} - \omega_h\right) |i_h|}{2} \right] \right\} \begin{bmatrix} -\sin \theta_{re} \\ \cos \theta_{re} \end{bmatrix} \tag{15}$$

4.2. Discrete-time super-twisting extended state observer

After the estimated extend EMFs are obtained in (15), the error of the rotor position $\tilde{\theta}$ can be either formulated by the heterodyne method or observed by the ELO introduced in Section 3. Finally, the rotor position and speed can then be estimated by a super-twisting extended state observer (STESO) in (16).

$$\begin{cases} \dot{\hat{\theta}}_{re} = \hat{\omega}_{re} + \alpha_1 \left| \theta_{re} - \hat{\theta}_{re} \right|^{\frac{2}{3}} sgn\left(\theta_{re} - \hat{\theta}_{re}\right) \\ \dot{\hat{\omega}}_{re} = a i^*_{\delta} + b i^*_{\gamma} i^*_{\delta} + \alpha_2 \left| \dot{\hat{\theta}}_{re} - \hat{\omega}_{re} \right|^{\frac{1}{2}} sgn\left(\dot{\hat{\theta}}_{re} - \hat{\omega}_{re}\right) + \hat{z} \\ \dot{\hat{z}} = \alpha_3 sgn\left(\dot{\hat{\theta}}_{re} - \hat{\omega}_{re}\right) \end{cases} \tag{16}$$

where a=1.5$P_n\lambda_f/J$; b=1.5$P_n(L_d - L_q)/J$; P_n is the number of pole pairs and λ_f is the permanent-magnet flux linkage. J is the equivalent moment of inertia. $\hat{z}$ represents the lump-sum of disturbances as the extended state. α_1, α_2 and α_3 are positive gains. Unlike the nonlinear extended state observer, the speed estimation errors are adopted

for the 2nd and 3rd order equations of STESO for robust estimation. The equivalent block diagram of the proposed 3rd STESO is presented in Fig. 2.

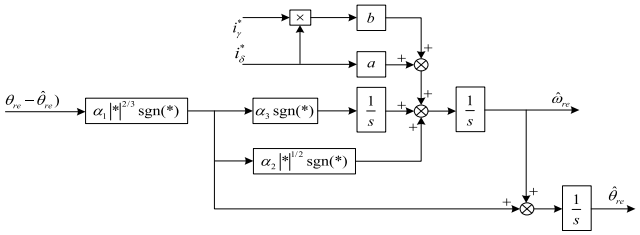

Fig. 2. Equivalent block diagram of the purposed 3rd order STESO.

In (16), the calculations of the 2nd and 3rd error terms are cumbersome. Hence, the following functions are introduced with the new coefficients k_1, k_2 and k_1 to simplify (16).

$$\begin{cases} f_1\left(\theta_{re}-\hat{\theta}_{re}\right)=k_1\left|\theta_{re}-\hat{\theta}_{re}\right|^{\frac{2}{3}}sgn\left(\theta_{re}-\hat{\theta}_{re}\right) \\ f_2\left(\theta_{re}-\hat{\theta}_{re}\right)=k_2\left|\theta_{re}-\hat{\theta}_{re}\right|^{\frac{1}{3}}sgn\left(\theta_{re}-\hat{\theta}_{re}\right) \\ f_3\left(\theta_{re}-\hat{\theta}_{re}\right)=k_3 sgn\left(\theta_{re}-\hat{\theta}_{re}\right) \end{cases} \tag{17}$$

Considering that one-step Euler method is easy to implement and computationally economical, discrete-time implementation of (17) is expressed as

$$\begin{cases} \hat{\theta}_{re}(k+1)=\hat{\theta}_{re}(k)+T_s f_\theta\left(\theta_{re}(k)-\hat{\theta}_{re}(k)\right)+T_s\hat{\omega}_{re}(k) \\ \hat{\omega}_{re}(k+1)=\hat{\omega}_{re}(k)+T_s f_\omega\left(\theta_{re}(k)-\hat{\theta}_{re}(k)\right)+T_s(ai_\delta^*+bi_\gamma^* i_\delta^*)+T_s\hat{z}(k) \\ \hat{z}(k+1)=\hat{z}(k)+T_s f_z\left(\theta_{re}(k)-\hat{\theta}_{re}(k)\right) \end{cases} \tag{18}$$

The system trajectories with T_s and upper bound of L are transferred onto the discrete-time domain. The discrete-time observer preserves the asymptotic properties of the original continuous-time one. Fig. 3 illustrates the overall structure.

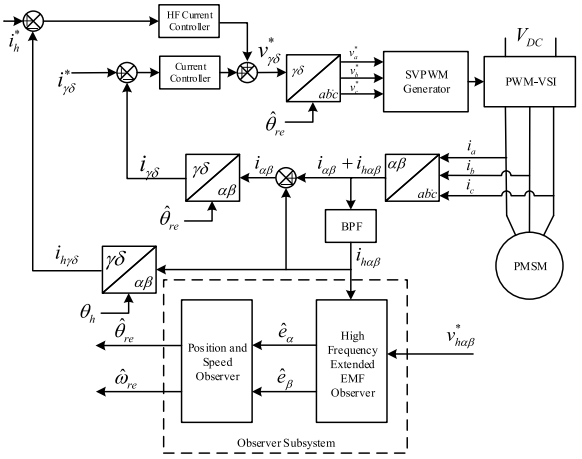

Fig. 3. Sensorless control diagram with HF injection.

5. Experimental results

A low-speed testing has been performed to verify the effectiveness of the HF extended EMF observer and the extraction ability of the STESO for position and speed estimation. The injection frequency was set to 800 Hz. A

test rig and an IPMSM were adopted for the experimental test. The testing was conducted on an ac motor hardware platform manufactured by dSPACE. The control platform, the inverter, and the Magtrol test bench are illustrated in Fig. 4. The switching frequency of the inverter was set to 10 kHz. The dead time was 2 μs. The speed and position feedback were closed with the estimated speed and position from the observers respectively. The real speed measured by the encoder and position estimation error were presented in the experiments. The parameters of the testing IPMSM are listed in table I [6].

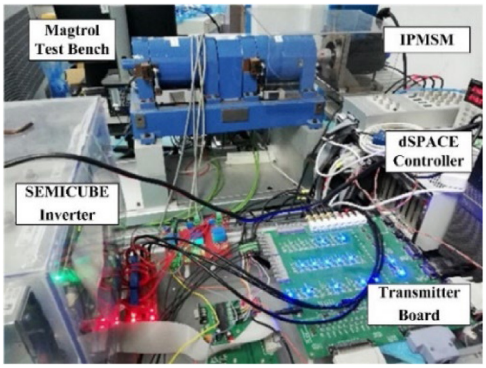

Fig. 4. Experiment test-rig setup.

5.1. Dynamic performance

The dynamic performance for extracting rotor position and speed is demonstrated with the HF extended EMF observer and the STESO. The amplitude of the injection current was 0.2 A. The machine speeded up from 5 rpm to 100 rpm under 5 N m load torque. The rotor speed and position performance are presented in Fig. 5. It is observed that the speed increased smoothly to 100 rpm with slight oscillations. The estimation error is significantly reduced after the acceleration period and contained under 0.2 rad.

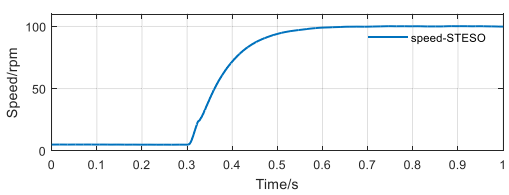

(a) Rotor speed by STESO

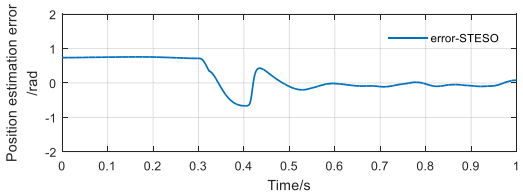

(b) Position estimation error

Fig. 5. The speed accelerated from 5 rpm to 100 rpm under light load with HF injection.

The estimated HF extended EMF and extracted fundamental extended EMF are shown in Fig. 6. The comparison of them are demonstrated to verify the effectiveness of the front end HF observer. The extracted fundamental components contain less oscillation and the frequency of that vary with increasing of the rotor speed.

5.2. Steady-state response

The IPMSM was operated at 30 rpm at full load condition. The injection current was set to 0.1 A. The responses was recorded in Fig. 7. It is found that the rotor speed generates ripples around 2 rpm. The estimation error was restricted below 0.3 rad. The estimated HF extended EMF and the extracted fundamental extended EMF are presented in Fig. 8.

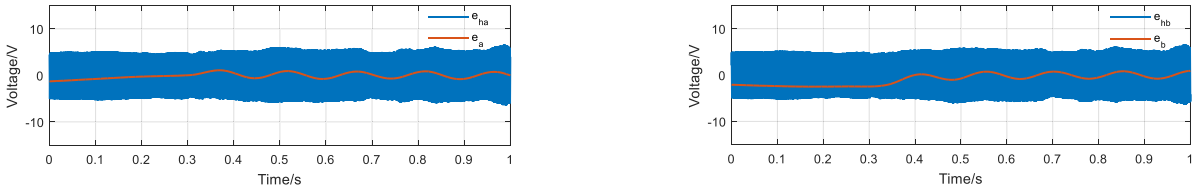

(a) $\hat{e}_{h\alpha}$ and $\hat{e}_{\alpha}$ (b) $\hat{e}_{h\beta}$ and $\hat{e}_{\beta}$

Fig. 6. Estimated HF extended EMF $\hat{e}_{h\alpha\beta}$ and extracted fundamental extended EMF $\hat{e}_{\alpha\beta}$ during the acceleration of the speed from 5 rpm to 100 rpm.

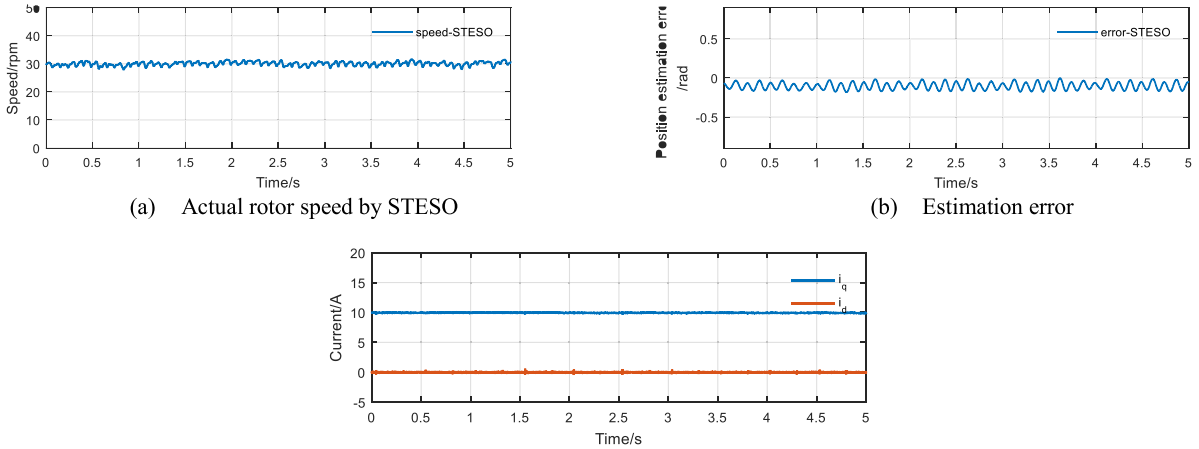

(a) Actual rotor speed by STESO (b) Estimation error

(c) Currents

Fig. 7. Steady-state operation at 30 rpm under full load.

(a) $\hat{e}_{h\alpha}$ and $\hat{e}_{\alpha}$ (b) $\hat{e}_{h\beta}$ and $\hat{e}_{\beta}$

Fig. 8. Estimated HF extended EMF $\hat{e}_{h\alpha\beta}$ and extracted fundamental extended EMF $\hat{e}_{\alpha\beta}$ at 30 rpm under full load.

5.3. Speed reversal test

The speed reverses between ± 20 rpm under light load condition. The speed performance and current response are presented in Fig. 9. The speed by STESO exhibits small oscillations around 3rpm and the transit duration is smooth. The i_q current response varies from $+2.5$ A to -2.5 A due to the speed reversal. Only small oscillations exist in the current response.

6. Conclusion

In this paper, a HF extended EMF has been proposed to achieve high performance in low speed sensorless operation. A HF observer estimates the extended EMF excited by the injection current. The design of the front-end observer has been presented and the stability has been analyzed. A close loop superimposed HF injection system is adopted to maintain the stable existence of the HF components and in the meanwhile avoid interrupt the original control loop. The proposed STESO retrieves the position and speed. The low speed experimental test has verified

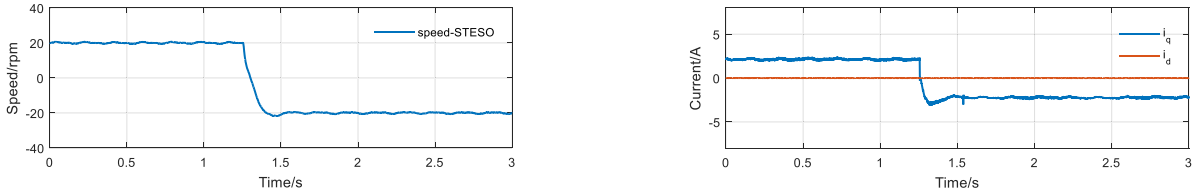

(a) Rotor speed by STESO (b) Current response

Fig. 9. Speed reversal between +20 rpm and −20 rpm produced by STESO.

the effectiveness of such method. Further, the research work on such method at low speed needs to be extended and improved. In-depth investigation on the selection for the amplitude and frequency of the injection current under different load conditions is to be performed. Improvement on the dynamic performance, machine startup and speed reversal can be conducted to enrich the content.

Declaration of competing interest

The authors declare that they have no known competing financial interests or personal relationships that could have appeared to influence the work reported in this paper.

Data availability

Data will be made available on request.

Acknowledgments

Supported by Ningbo Science and Technology Bureau, China under the project No. 202003N4182.

References

[1] Yu Linxin, Wang Dazhi, Zheng Di, Liu Zhen, Ji Mengran. Performance improvement of PMSM rotor position estimation by using adaptive hybrid filter based PLL. Energy Rep 2021;7(Supplement 6):515–21.
[2] Huo J, Zhao N, Gao R, Zhang G, Wang G, Xu D. Analysis and compensation of position estimation error for sensorless reduced DC-link capacitance IPMSM drives. IEEE Trans Ind Electron 2022. http://dx.doi.org/10.1109/TIE.2022.3170637.
[3] Dianov A. Highly efficient sensorless multi control mode compressor IPMSM drive with seamless transitions. IEEE Trans Power Electron 2022. http://dx.doi.org/10.1109/TPEL.2022.3157476.
[4] Yoo J, Kim H-S, Sul S-K. MTPA tracking control of sensorless IPMSM based on square-wave voltage signal injection. IEEE Trans Power Electron 2022. http://dx.doi.org/10.1109/TPEL.2022.3179241.
[5] Gou L, Wang C, You X, Zhou M, Dong S. IPMSM sensorless control for zero- and low-speed regions under low switching frequency condition based on fundamental model. IEEE Trans Transp Electr 2022;8(1):1182–93. http://dx.doi.org/10.1109/TTE.2021.3093069.
[6] Xu Z, Zhang T, Gerada C. A PMSM with enhanced anisotropic rotor configuration for sensorless operations. IEEE Trans Energy Convers 2021;36(4):2872–83. http://dx.doi.org/10.1109/TEC.2021.3069096.
[7] Ishii Y, Yamashita H, Kubota H. A quiet position sensorless control for an IPMSM based on extended EMF and voltage injection synchronized with PWM carrier. In: 2018 International power electronics conference. (IPEC-Niigata 2018 -ECCE Asia), 2018, p. 1196–201.
[8] Xu Z, Rahman MF. An adaptive sliding stator flux observer for a direct-torque-controlled IPM synchronous motor drive. IEEE Trans Ind Electron 2007;54:2398–406.
[9] Gou L, Wang C, You X, Zhou M, Dong S. IPMSM sensorless control for zero- and low-speed regions under low switching frequency condition based on fundamental model. IEEE Trans Transp Electr 2022;8(1):1182–93. http://dx.doi.org/10.1109/TTE.2021.3093069.